



Three-dimensional arrangements of perovskite-type oxide nano-fiber webs for effective soot oxidation



Chanmin Lee^{a,1}, Yukwon Jeon^{b,1}, Satoshi Hata^c, Joo-Il Park^d, Ryutaro Akiyoshi^a, Hikaru Saito^e, Yasutake Teraoka^a, Yong-Gun Shul^{b,**}, Hisahiro Einaga^{a,f,*}

^a Department of Molecular and Material Sciences, Interdisciplinary Graduate School of Engineering Sciences, Kyushu University, Kasuga, Fukuoka, 816-8580, Japan

^b Department of Chemical and Biomolecular Engineering, Yonsei University, Yonsei-ro 50, Seodaemun-gu, Seoul, 120-749, Republic of Korea

^c Department of Electrical and Materials Science, Faculty of Engineering Sciences, Kyushu University, Kasuga, Fukuoka 816-8580, Japan

^d Petroleum Research Center, Kuwait Institute for Scientific Research (KISR), P.O. Box 24885 Safat, 13109 Kuwait

^e Center of Advanced Instrumental Analysis, Kyushu University, Kasuga, Fukuoka, 816-8580, Japan

^f Department of Energy and Material Sciences, Faculty of Engineering Sciences, Kyushu University, Kasuga, Fukuoka 816-8580, Japan

ARTICLE INFO

Article history:

Received 14 December 2015

Received in revised form 25 February 2016

Accepted 2 March 2016

Available online 4 March 2016

Keywords:

LaSrCoFeO₃ perovskite oxide

Nano-fibrous catalyst

Diesel soot combustion

Electrospinning

Electron tomography

ABSTRACT

Perovskite-type oxides have been widely applied in heterogeneous catalytic reactions, such as soot oxidation. However, a poor contact point between the catalyst and solid reactant (soot) often limits the catalytic performance. Here, we report La_{1-x}Sr_xCo_{0.2}Fe_{0.8}O_{3-δ} perovskite oxide catalysts with a unique three-dimensional (3D) fiber web structure that increases the high-contact area by trapping soot in the unique pore structure for effective catalytic activity. This feature was carefully analyzed using scanning transmission electron microscopy (STEM) tomography to investigate the location of the soot on the web. The structure of the web, with a thickness of approximately 55 μm, indicated that the soot particles were caught by the 3D pores between the fibers. The relationship between the Sr amount and active oxygen was also characterized by means of XPS. The results show that the Sr amount of 0.4 produced the highest amount of active oxygen species (O⁻) that are essential for soot oxidation reaction. The developed catalyst exhibited a good catalytic performance due to the optimized perovskite chemical structure and the greatly increased number of the contact points owing to the 3D inter-fiber spaces. Hence, our proposed approach is reasonable for application to real soot combustion processes and can also be easily extended to numerous other catalytic processes to enhance the catalytic activity.

© 2016 Elsevier B.V. All rights reserved.

1. Introduction

To control the emission of fine particulate matter (PM, diameter of 2.5 μm or less) from diesel engines, which consists mainly of soot (carbon) and is known to be a dangerous carcinogen [1], a continuously regenerating diesel particulate filter (CRDPF) that uses catalytic processes and physically traps soot has been proposed as an effective after-treatment system [2–5]. Therefore, various

catalysts have been intensively investigated for soot oxidation combustion, such as ceria-based materials [6–8], precious metal [9], alkali-metal oxides [10–12], spinel oxides [13,14] and perovskite or perovskite-related oxides [15–17]. Among these catalysts, perovskite oxides, which have a general formula structure of ABO₃, have recently been exploited as catalysts for soot oxidation because of their high thermal stability and intrinsic catalytic activity [18]. In particular, perovskite-type oxides containing alkaline and alkaline earth metals have been reported to exhibit high catalytic activity for soot combustion [19,20]. However, these oxides are relatively unstable at high temperature and are decomposed during catalytic soot oxidation [21].

It has been reported that ABO₃ perovskite-type oxides containing Co at B sites exhibits high catalytic oxidation activities. Moreover, the doping of transition metals to the A and B sites improves the oxidation activity. For instance, the substitution of trivalent cations La³⁺ at A sites of LaCoO₃ by divalent cation gener-

* Corresponding author at: Department of Energy and Material Sciences, Faculty of Engineering Sciences, Kyushu University, Kasuga, Fukuoka, 816-8580, Japan.

** Corresponding author at: Department of Chemical and Biomolecular Engineering, Yonsei University, Yonsei-ro 50, Seodaemun-gu, Seoul, 120-749, Republic of Korea, Republic of Korea.

E-mail addresses: shulyg@yonsei.ac.kr (Y.-G. Shul), einaga.hisahiro.399@m.kyushu-u.ac.jp (H. Einaga).

¹ These authors contributed equally.

ates oxygen vacancies and/or changes the oxidation state of B site cations, giving rise to the increase in the lattice oxygen mobility and oxygen desorption, which are related with catalytic oxidation properties [22]. Teraoka et al. have also reported that Fe substitution for B site cations of $\text{La}_{1-x}\text{Sr}_x\text{CoO}_{3-\delta}$ series oxides enhances the oxygen desorption properties [23–26]. Partial substitution of cations at the B sites also improved the activity for catalytic oxidation [27,28].

The activity of a heterogeneous catalyst also largely depends on the number of contact points between the catalyst surface and solid reactant (soot). Generally, the pore size of the prevalent catalyst (less than 10 nm) is smaller than the diameter of soot (greater than 25 nm), which often limits the catalytic soot oxidation [29] because soot cannot penetrate the inner pores of the catalyst [30]. To increase the catalyst-soot contact area, several methods have been proposed over the past few decades, including the use of three-dimensionally ordered macroporous (3DOM) oxides (pore size >50 nm) [31–33], in addition to oxides in the form of shape-controlled cubes, rods (polyhedral and/or non-polyhedral shapes) [34,35] and fiber structures [36,37]. Despite many attempts to enhance the catalytic performance by increasing the contact area, only limited applications in real filter systems have been demonstrated.

In this paper, we present a novel perovskite nano-fiber web with 3-dimensional structures, which can increase the contact area between the nano-fibers and soot particles and enable efficient trapping of soot particles and their combustion. Morphological observations of the location of soot were performed, for the first time, using three-dimensional (3D) electron tomography from various points of view. $\text{La}_{1-x}\text{Sr}_x\text{Co}_2\text{Fe}_8\text{O}_{3-\delta}$ perovskite fibrous webs with different Sr doping levels were produced using an electrospinning technique [38] to achieve a unique matrix morphology with a hierarchical porous structure. To verify the effect of the novel fiber web structure on the catalytic activity, we compared the diesel oxidation performance of the developed novel perovskite nano-fiber web catalyst with that of a $\text{La}_{1-x}\text{Sr}_x\text{Co}_{0.2}\text{Fe}_{0.8}\text{O}_{3-\delta}$ bulk-type catalyst.

2. Experimental

2.1. Materials and synthesis of LaSrCoFeO_3 nanofibrous webs

Polyvinylpyrrolidone (PVP, MW = 1,300,000), Ethanol ($\text{C}_2\text{H}_6\text{O}$, 99.9%), *N,N*-dimethylformamide (DMF, 99.9%) and Iron nitrate nonahydrate ($\text{Fe}(\text{NO}_3)_3 \cdot 9\text{H}_2\text{O}$) were purchased from Sigma-Aldrich Co., Ltd. (USA). Cobalt nitrate hexahydrate ($\text{Co}(\text{NO}_3)_2 \cdot 6\text{H}_2\text{O}$) and Strontium nitrate ($\text{Sr}(\text{NO}_3)_2$) were obtained from Junsei Chemical Co., Ltd. (Japan). Lanthanum nitrate hexahydrate ($\text{La}(\text{NO}_3)_3 \cdot 6\text{H}_2\text{O}$) was supported by Yakuri Pure Chemicals Co., Ltd. (Japan). La-Sr-Co-Fe (LSCF) type mixed oxide nano-fibers were synthesized by an electrospinning method. Metal nitrates in stoichiometric ratios ($\text{La}_{1-x}\text{Sr}_x\text{Co}_{0.8}\text{Fe}_{0.2}$, $x = 0.2, 0.3$ and 0.4) were dissolved in a mixed solution of dimethylformamide (DMF) and ethanol with the weight ratio of 8:2. Here, the weight ratio of the mixture to the solvent was 1:4.67. After stirring for 1 h, polyvinylpyrrolidone (PVP; MW = 1,300,000) was added at a weight ratio of 1:1.5 of PVP and metal nitrates. Then, this precursor solution was homogenized via vigorous stirring for 6 h at room temperature. This solution was judiciously electrospun using a high voltage of 18 kV, and a feed flow of 1.2 mL h^{-1} was applied to produce a nano-fiber. The tip size was 30 G (0.15 mm inner diameter), and the distance between the tip and the drum collector, which was constantly rotated (150 rpm, revolution per minute), was 15 cm. The humidity and temperature were kept below 30% RH and approximately 35 °C, respectively, during the electrospinning. Subsequently, the electrospun LaSr-CoFe (LSCF) precursor/PVP composite fibers were heated at 800 °C

in an air atmosphere for 6 h at a rate of 1°C min^{-1} to completely remove nitrate and polymeric ingredients (PVP) and enable bonding and fusion of the particles.

2.2. Catalyst characterization

The fiber diameter and shape were analyzed using SEM images and energy dispersive spectroscopy (EDS) mapping using a JSM-6710F (JEOL, Japan). To study the morphology, TEM imaging and EDS mapping were performed using a JEM-ARM 200F (JEOL) at 200 eV. To further study the 3D web structure, STEM tomography observations were performed using a FEI Titan G2 60–300 at 300 kV. The images were recorded in the range of -68 to $+62$ with approximately 2 tilt angle intervals. XRD patterns were measured with an RINT 2000 (RIGAKU, Japan) instrument using Co-K α radiation (1.79 Å). The chemical compositions were characterized using XPS (Thermo VG Scientific, UK). XPS spectra were collected using a K-alpha apparatus under vacuum (7.8×10^{-9} mbar); for these measurements, a monochromatic, Al X-ray source (Al-K α line at 1486.6 eV) was utilized. To study the porous structure, nitrogen physic-sorption analysis was performed using a BELSORP II (BEL, Japan) apparatus at -196°C . Before the measurement, the samples were degassed at 200°C for 3 h under vacuum condition to remove moisture. The macropore size distributions were obtained by mercury intrusion analysis using a Micromeritics Atuopore III (SHIMADZU, Japan) instrument.

2.3. Soot oxidation measurements

To perform soot oxidation, the catalyst and 5-wt% carbon black (CB, Sigma-Aldrich), as a simulated soot substance, were mixed using a spatula and an agate mortar for 10 min under the LC and TC modes [36]. The soot oxidation reactions were performed using TGA (Shimadzu DTG-60) in an air atmosphere (21% O_2 and 79% N_2 , 100 mL min^{-1}). The temperature range was 120 – 800°C , and the heating rate was $10^\circ\text{C min}^{-1}$, respectively. The measured values were the following: (I) ignition temperature (T_{ig}), (II) highest temperature (T_{max}) and (III) finishing temperature (T_f). When two T_{max} peaks were observed, the higher temperature was designated as $T_{max,L}$, and the lower temperature was defined as $T_{max,H}$. Temperature programmed oxidation (TPO) for catalyst-carbon black mixture was carried out using a fixed-bed flow reactor. The mixture of soot and catalyst was heated from 100 to 700°C at a heating rate of $10^\circ\text{C min}^{-1}$ in a 100 mL min^{-1} gas flow of 6% O_2 and 3% H_2O (or without H_2O) in N_2 . CO_2 concentration in exhaust gas was measured by FT-IR spectrometer (Perkin-Elmer, spectrum 100).

2.4. Activation energy

The activation energy (ΔE) was calculated by applying the Ozawa method to the TGA data [39,40]. For the measurement, mixtures of catalyst and soot (95:5 weight ration) were characterized in a reaction temperature range of 120 – 180°C under an air atmosphere. The heating rates (Φ) were 5, 10, 20, and $30^\circ\text{C min}^{-1}$; according to the Ozawa method, the values of the absolute temperature (T_α) at which a fixed fraction occurred were obtained from the resultant TG curves. The activation energy was calculated from the least-squares fit to the $\log \Phi$ versus T_α^{-1} data according to the following equation:

$$\log \Phi = B - 0.4567 \left(\frac{E_a}{RT_\alpha} \right)$$

where B is a constant value, R is the ideal gas constant value, and E_a is the activation energy of the reaction.

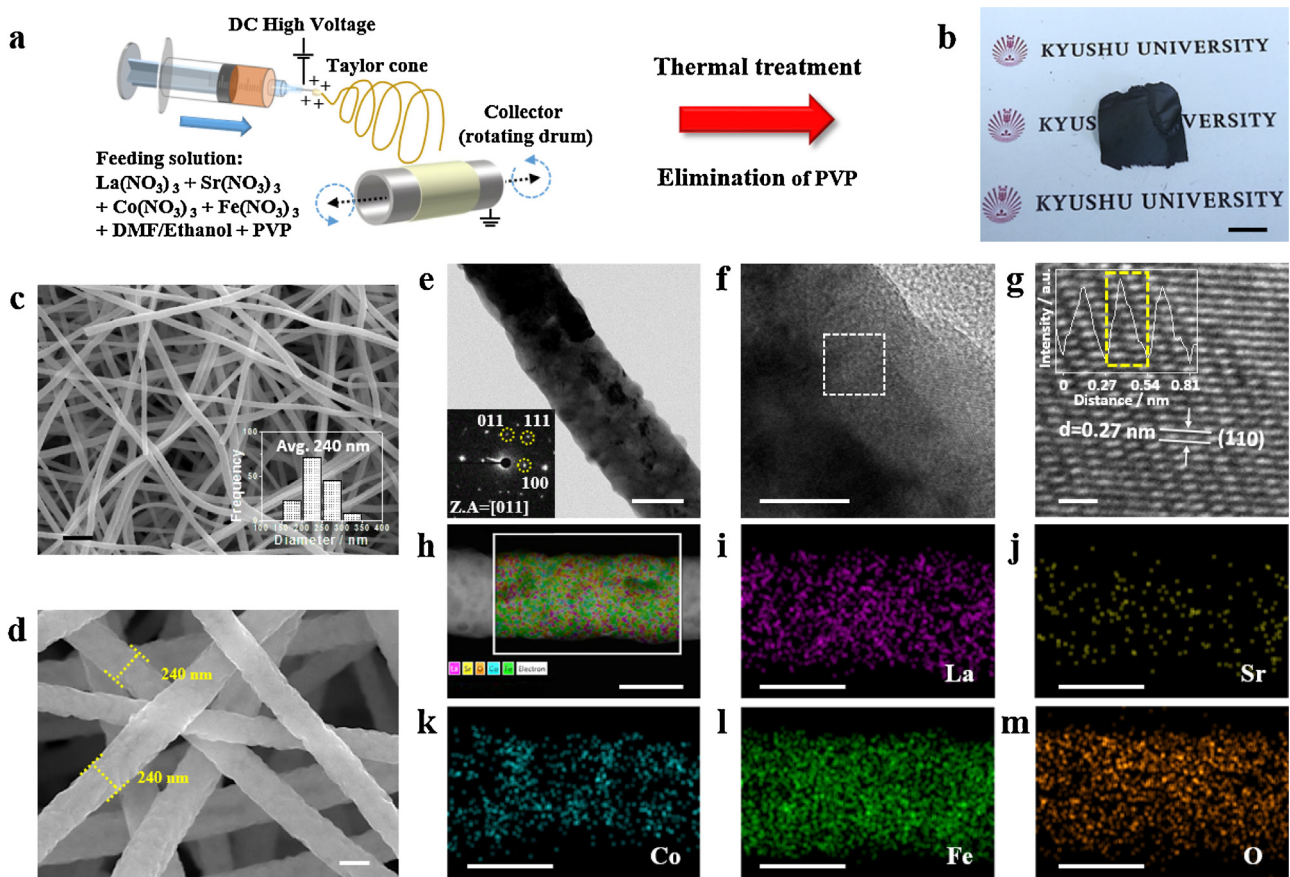


Fig. 1. Schematic illustration and morphological characterization of the electrospun LSCF6428-web. (a) The synthesis process of fabricating LSCF nano-fibers via the electrospinning method and subsequent calcination. (b) Digital photograph of the $\text{La}_{0.6}\text{Sr}_{0.4}\text{Co}_{0.2}\text{Fe}_{0.8}\text{O}_3$ fiber web calcined at 800 °C. Scale bar, 1 cm. (c and d) SEM image of $\text{La}_{0.6}\text{Sr}_{0.4}\text{Co}_{0.2}\text{Fe}_{0.8}\text{O}_3$ (LSCF6428) nano-fibers (insert: fiber diameter distribution). Scale bars, 1 μm (c) and 200 nm (d). (e) Bright-field STEM image of LSCF6428 (insert: SAED pattern). Scale bar, 100 nm. (f and g) HRTEM images of LSCF6428 (insert: line profile). Scale bar, 20 nm (f) and 1 nm (g). (h-m) Dark-field STEM image and EDX elemental mapping results for the LSCF-6428 fiber. Scale bar, 100 nm.

3. Results and discussion

3.1. Synthesis and characterization of $\text{La}_{1-x}\text{Sr}_x\text{Co}_{0.2}\text{Fe}_{0.8}\text{O}_{3-\delta}$ perovskite fibre webs

Macroporous $\text{La}_{1-x}\text{Sr}_x\text{Co}_{0.2}\text{Fe}_{0.8}\text{O}_{3-\delta}$ fibrous webs with different stoichiometric ratios ($x = 0.2 \sim 0.4$) (hereafter, these catalysts are denoted as LSCF6428-web, LSCF7328-web and LSCF8228-web) were prepared by electrospinning and subsequent calcination, as shown in Fig. 1a. Although this process is based on the normal synthesis of 1D inorganic fiber structures [37], we accumulated the fiber structure layer by layer to form a fibrous web with a hierarchical porous structure, which can capture soot in the inter-fiber spaces (Fig. 1b). For comparison, bulk-type perovskites of the same stoichiometric ratios were synthesized following a published procedure to investigate the effect of the web structure with the 3D pores (hereafter, these bulk-type perovskite catalysts are denoted as LSCF6428-bulk, LSCF7328-bulk and LSCF8228-bulk). Fig. 1c and d show the morphology of the LSCF fiber obtained, as determined by scanning electron microscopy (SEM) images. After heat treatment at 800 °C, the calcined LSCF fibers exhibited an average diameter of approximately 240 nm; the thickness of the LSCF web was approximately 55 μm (Fig. 4e). This structure was further confirmed by scanning transmission electron-microscopy (STEM) and high-resolution transmission electron microscopy (HRTEM), as shown in Fig. 1e-g and Supplementary Figs. S1–2. As indicated by Fig. 1g and the line profile shown in the inset, the spacing of the lattice fringes was 0.27 nm, corresponding to the (110) plane of

the LSCF perovskite structure. The selected area electron diffraction (SAED) pattern of LSCF6428-web also shows the [011] zone axis (Z.A) of the typical perovskite structure (insert Fig. 1e). Moreover, a homogeneous distribution of the La, Sr, Co, Fe and O atoms within the fiber was confirmed by the STEM-mode energy-dispersive X-ray spectroscopy (EDS) elemental mapping (Fig. 1h–m).

To investigate the structural characterizations, X-ray diffraction (XRD) studies were performed for the LSCF6428-web, LSCF7328-web and LSCF8228-web catalysts. The observed XRD patterns in Fig. 2a show the major diffraction peaks of (110), (111), (200), (210), (211), (220) and (310), indicating the cubic perovskite phase (JCPDS No. 01-089-5720). In general, $\text{La}_{1-x}\text{Sr}_x\text{Co}_{0.2}\text{Fe}_{0.8}\text{O}_{3-\delta}$ exhibits a cubic structure with a deficiency of Sr; moreover, rhombohedral perovskite crystallizes at low temperatures, from 600 to 800 °C, whereas approximately 90% of the above 1000 °C calcined $\text{La}_{1-x}\text{Sr}_x\text{Co}_{0.2}\text{Fe}_{0.8}\text{O}_{3-\delta}$ changed from a cubic to a rhombohedral form [41]. The magnified XRD image (on the right-hand side) shows detailed information about (110) and the d value for different La and Sr ratios. The angle of the (110) reflection decreased with increased Sr content from 32.37° in LSCF6428-web to 32.22 and 32.15° in LSCF7328-web and LSCF8228-web, respectively, whereas the d value (basal spacing) increased from 2.763 Å to 2.776 and 2.782 Å. In addition, the a , b and c axis cell parameters also increased from 3.899 to 3.915 Å and 3.923 Å, as indicated in Supplementary Table S1. These changes implied that the different dimensions of the perovskite unit cell are attributed to the different crystal ionic radii by partial substitution of La with Sr ion in the A site.

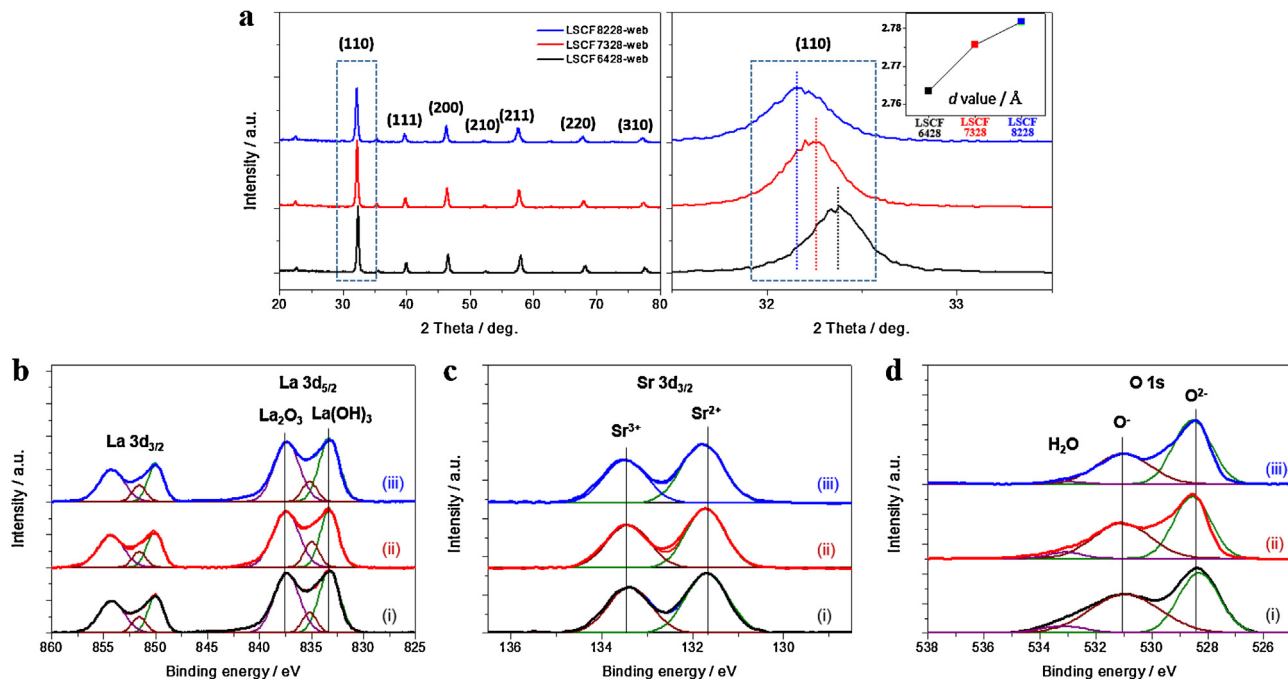


Fig. 2. Chemical composition analysis of web type. (a) XRD patterns and XPS results for the LSCF-web types: (b) La 3d, (c) Sr 3d and (d) O 1s spectra ((i): LSCF6428-web, (ii): LSCF7328-web and (iii): LSCF8228-web).

X-ray photoelectron spectroscopic studies were also conducted to study the structural changes caused by the variations in the La and Sr content at the A site. Fig. 2b-d and Supplementary Fig. S3 represent the XPS spectrum of LSCF6428-web, LSCF7328-web and LSCF8228-web corresponding to La 3d, Sr 3d, Co 2p, Fe 2p and O 1s. Regarding the La and Sr species, two similar peaks of La 3d_{5/2} and La 3d_{3/2} were identified in the La 3d region; these were related to not only the La³⁺ oxide phase (833.1–833.3 eV) but also a lower-oxidation state (837.3–837.5 eV) because of hydroxyl group formation [42] (Fig. 2b). In the Sr 3d region, the typical two peaks were split at 131.8 ± 0.1 and 133.5 ± 0.1 eV, which are associated with Sr in a perovskite and a sub-oxide phase, respectively (see Fig. 2c) [43]. The fitted binding energies and calculated atomic ratios are listed in Supplementary Table S2. It is clearly seen that the oxidation state increased for both La and Sr as the Sr doping level increased. These structural changes influenced the oxygen configuration in the perovskite structure, which is highly related to the soot combustion activity. In Fig. 2d, the O 1s spectra was fitted with two peaks: one at a low binding energy of 528.3–528.6 eV associated with lattice oxygen (O²⁻), and the other at a binding energy of 531.0–531.1 eV related to surface adsorbed oxygen (O⁻), which is generally known to be important for the oxidation reaction [43]. To confirm whether the soot oxidation was favorable, we estimated the ratio of O_{surface}/O_{lattice} for LSCF6428-web, LSCF7328-web and LSCF8228-web. The O_{surface}/O_{lattice} ratios were 1.11, 0.88, and 0.68 for LSCF6428-web, LSCF7328-web and LSCF8228-web, respectively. It is likely that the increase in Sr doping levels increased the amount of oxygen vacancy, which is related with the catalytic properties of perovskite oxides [44–46].

3.2. Analysis of the 3D porous structure

To understand the effect of the 3D nano-fiber perovskite web on the surface and pore-structure properties, Brunauer–Emmett–Teller (BET) surface area and Barrett, Joyner and Halenda (BJH) pore size distributions were determined from the N₂ adsorption–desorption isotherms and shown in Fig. 3. Both LSCF6428-web and LSCF6428-bulk exhibit type III isotherms and H3 hysteresis loops,

corresponding to a mesoporous (with a pore size of 2–50 nm) configuration and a significantly wide pore size distribution (Fig. 3a) [47]. This result was supported by the BJH pore size distribution (Fig. 3b). Two identical peaks at ~2 nm and 10–50 nm were observed; these peaks correspond to microporous and large mesoporous structures, respectively. BET surface area of the LSCF webs were calculated to be in the range of 7.9–7.4 m² g⁻¹, whereas the LSCF bulks have lower surface areas (4.1–5.5 m² g⁻¹).

To further investigate the detailed pore structure of the inter-fibers and inter-particles, mercury intrusion analysis was also performed on the LSCF web and bulk types. As shown in Fig. 3c, the pore distribution of LSCF6428-web was observed to span approximately 1–90 μm, whereas that of LSCF6428-bulk was distributed at only approximately 1 μm. Similar pore size distributions of 1–90 μm for LSCF7328-web and LSCF8228-web and 1 μm for LSCF7328-bulk and LSCF8228-bulk were observed (Supplementary Fig. S4b). The total intrusion volumes of LSCF6428-web and LSCF6428-bulk were also different, with values of 3.67 and 0.78 mL g⁻¹, respectively.

To visualize the 3D morphological characterization of the web structure, SEM, EDS mapping, STEM and electron tomography analysis were conducted. First, for soot catalytic oxidation, a 5 wt% carbon black (average diameter of approximately 35 nm, Supplementary Fig. S5), as a model substance of diesel soot, and the prepared catalyst were mixed using a previously developed universally used method [36]. We used both the loose-contact (LC) and tight-contact (TC) modes between the soot particle and catalyst on the surface, even though the LC mode is generally utilized for actual filters, as shown in Fig. 4a [48–50]. For practical conditions, Fig. 4b-d show SEM images of LSCF6428-web before and after capture of the soot particles in the LC mode. When the contact point between the soot and the catalyst in the bulk type was only observed on the surface, the contact in the web type was observed not only on the surface but also at the interspaces between perovskite fibers, as also confirmed by Supplementary Figs. S1 and S6. Fig. 4e-g exhibit cross-sectional SEM and EDS mapping images of the mixture of the LSCF6428-web with soot, indicating the presence of carbon (red spots) due to the soot particles being

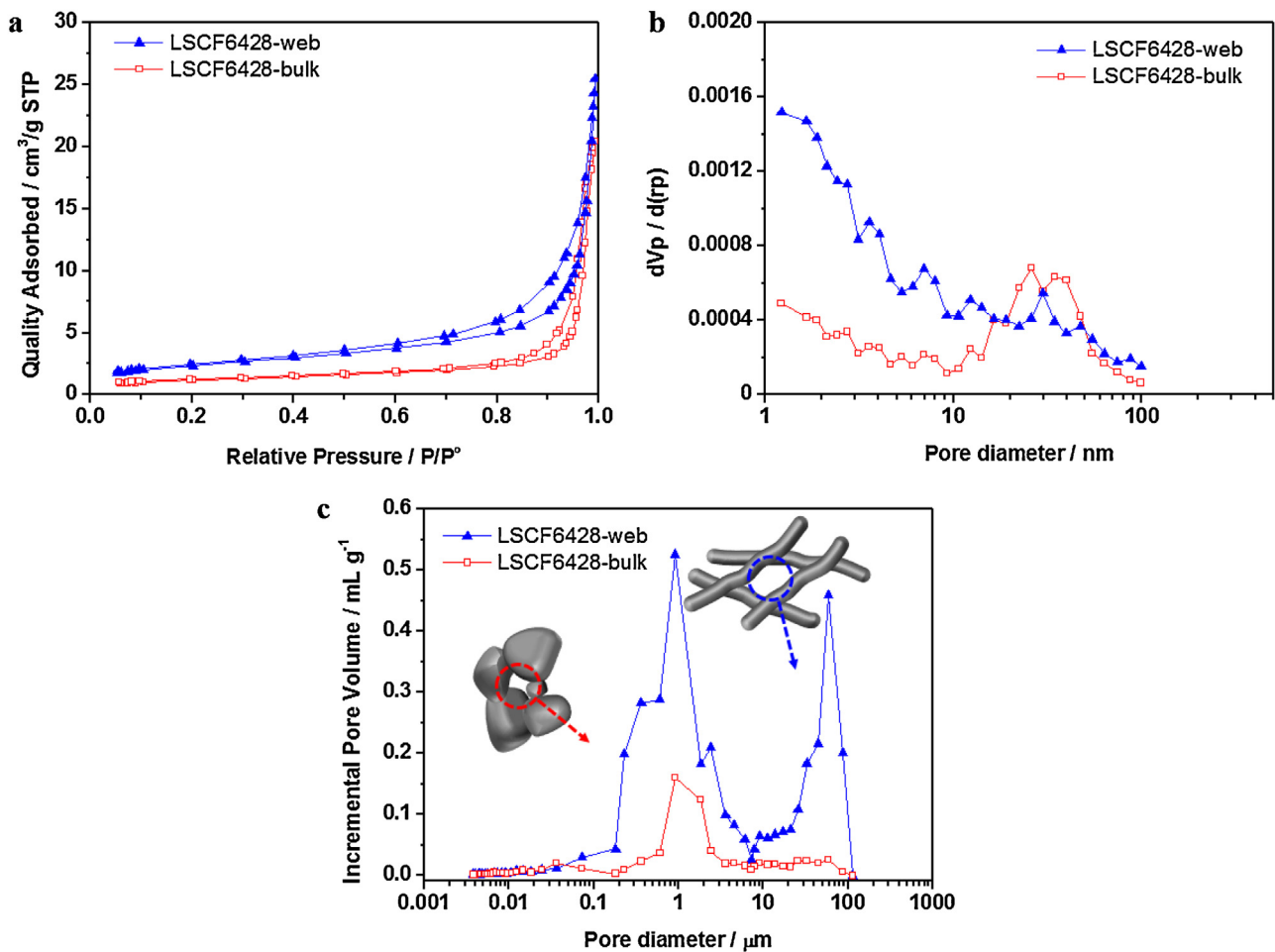


Fig. 3. Study of the pore structures of the LSCF6428-web (blue) and LSCF6428-bulk (red) types on the surface and interspaces between materials (particles or fiber web). (a) N₂ adsorption-desorption isotherm. (b) BJH pore size distribution. (c) Pore size distribution obtained from mercury porosimetry measurements. (For interpretation of the references to color in this figure legend, the reader is referred to the web version of this article.)

engaged within the interspaces of the synthesized perovskite fiber web.

We performed STEM imaging, electron tomography and EDS mapping to further confirm the 3D structural properties. Fig. 4h and Supplementary Figs. S7–8 exhibit STEM and electron tomography images, for which the specimen-tilt angle was varied from +60 to –60°. From Supplementary Figs. S1 and S6, the inter-fiber distances, which were created by overlapping fibers, covered a wide range, from approximately 400 nm to 2.5 μm. We assumed that their spaces were sufficiently able to catch the soot particles (less than 2.5 μm). For a detailed discussion of the internal contact positions between the soot and the web, additional 3D reconstructions using the simultaneous iterative reconstructive technique (SIRT) [51] and different specimen-tilt angles (from –68 to +62) are presented in Fig. 4i and j and Supplementary Fig. S6. In these 3D reconstructions, note that two types of contact types were found: in the first type, soot particles were positioned on the surface, whereas in the other, soot was located in the interspaces of the fiber-web (black and violet parts indicate soot and fibers, respectively). In particular, this web structure maintained a state that physically trapped the soot (see Supplementary Video).

3.3. Soot oxidation activity

The soot oxidation performance was evaluated via thermogravimetric analysis (TGA) using mixtures of carbon black and catalyst. Although examining soot catalytic oxidation using TC and

Table 1
Surface characterization and catalytic oxidation performance in the LC mode.

Sample	T _{ig} ^a (°C)	T _{max,L} ^b (°C)	T _{max,H} ^c (°C)	T _f ^d (°C)	S _{BET} ^e (m ² g ⁻¹)
LSCF-6428-web	397	490	585	647	7.9
LSCF-7328-web	403	494	590	650	7.7
LSCF-8228-web	413	505	597	655	7.4
LSCF-6428-bulk	429	–	623	677	4.1
LSCF-7328-bulk	432	–	624	681	4.1
LSCF-8228-bulk	436	–	629	684	5.5

^a T_{ig} (starting temperature of soot ignition).

^b T_{max} (maximum temperature).

^c T_{max,L} (lower maximum temperature).

^d T_f (finished temperature of soot oxidation).

^e Specific surface area (BET).

LC modes is a general method for evaluating the soot oxidation performance [36,48–50], we focused more on the LC mode because this is used for real filter systems. First, Fig. 5 shows the typical TG and DTA curves for soot oxidation of LSCF6428-web, LSCF7328-web, LSCF8228-web, LSCF6428-bulk, LSCF7328-bulk and LSCF8228-bulk in the LC mode [46]. The measured values of T_{ig}, T_{max}, T_{max,L}, T_{max,H} and T_f are presented in Table 1. As indicated by Fig. 5b and Table 1, in the case of the bulk structures, the T_{ig} (ignition temperature) values of LSCF6428-bulk, LSCF7328-bulk and LSCF8228-bulk were measured to be 429, 432 and 436 °C, respectively; the T_{max} values of LSCF6428-bulk, LSCF7328-bulk and LSCF8228-bulk were measured to be 623, 624 and 629 °C (Fig. 5b, inset), respectively; and

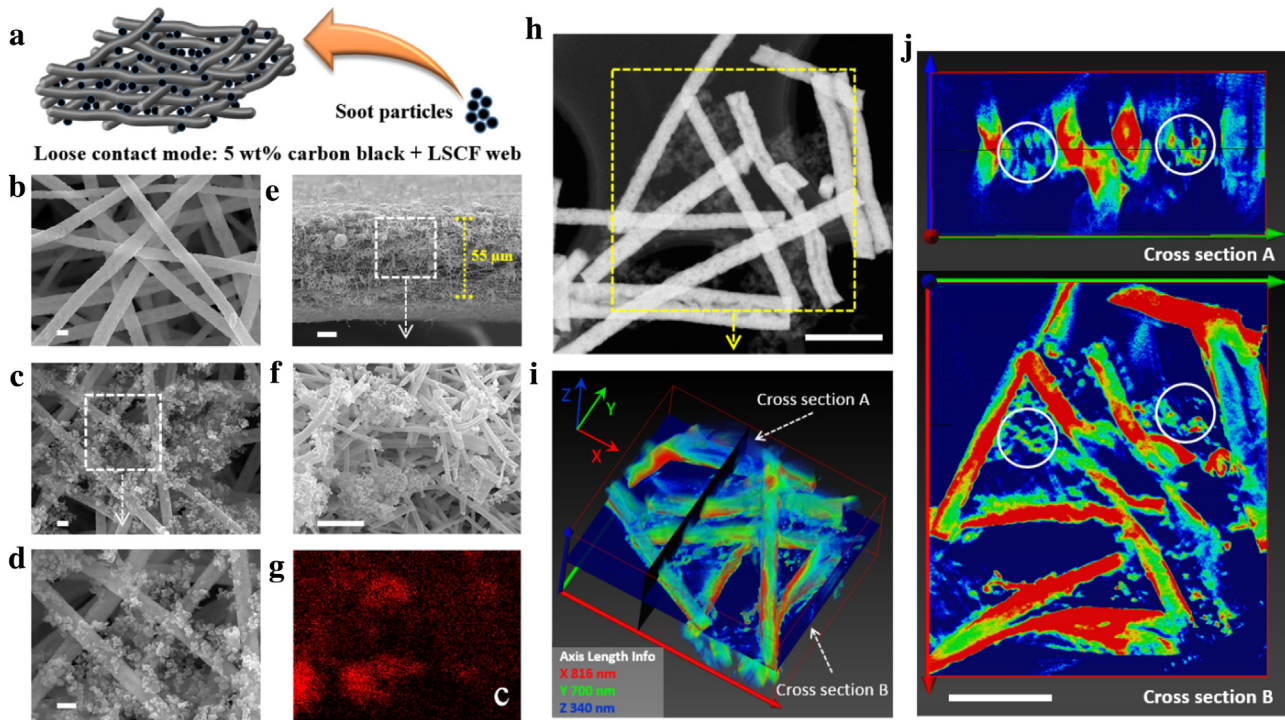


Fig. 4. Analysis of the mixture of soot and LSCF6428-web in the LC mode (between soot and catalyst) to determine the catalytic performance. A mixture of 5 wt% carbon black and LSCF6428-web was prepared using the LC mode, and was mixed using a spatula. (a) Fabrication of the mixture step. (b–d) SEM images of a surface section. Scale bar, 200 nm. (e) SEM image of a cross-section. Scale bar, 10 μ m. (f–g) EDS mapping image. Scale bar, 2.5 μ m. (h) STEM dark-field images of the mixture. Scale bar, 200 nm. (i) 3D model reconstructed from the STEM tomography results. (j) Cross-sections of tomographic reconstruction image in two directions. Scale bar, 200 nm.

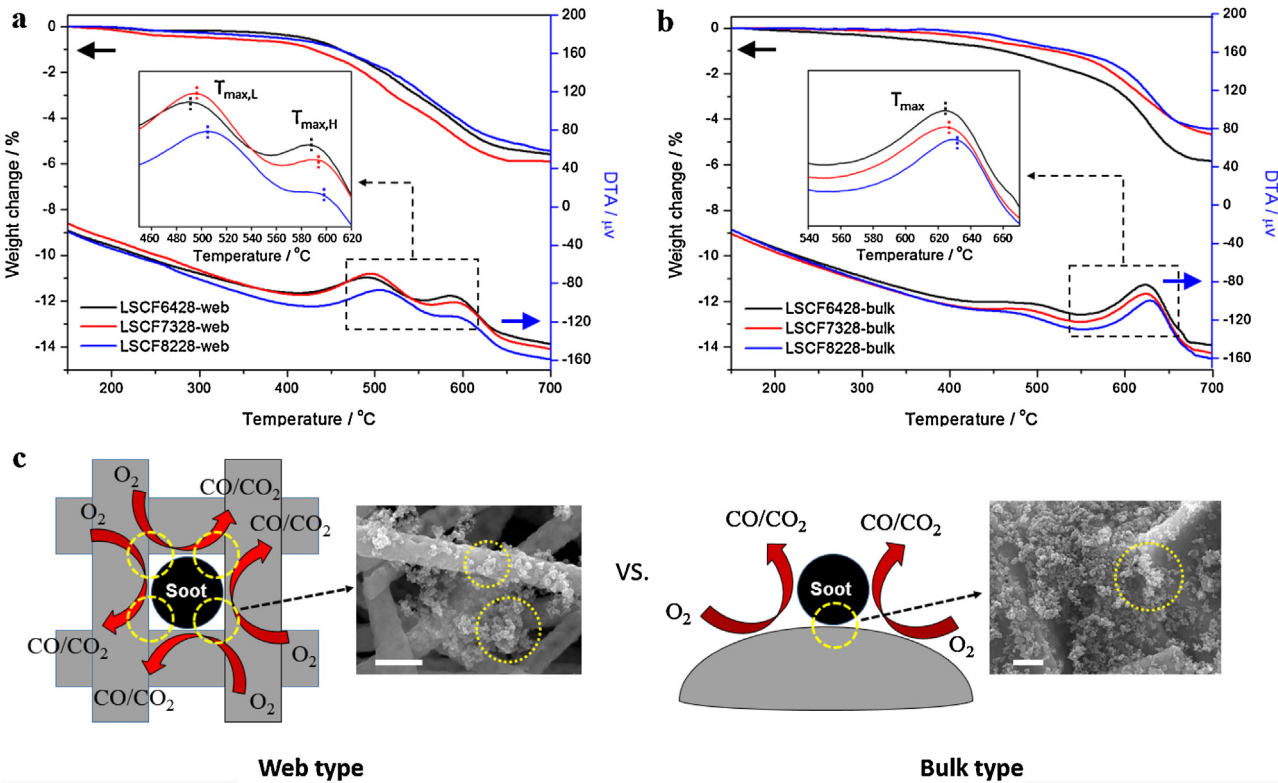


Fig. 5. Catalytic activities of the LSCF web and bulk types in the LC mode. TG and DTA curves of the LSCF (a) web and (b) bulk types; a mixture of 5 wt% carbon black and catalyst was used for the LC mode. (c) Schematic illustration of the soot oxidation process and surface SEM images. Scale bar, 500 nm.

the T_f values were determined to be 677, 681 and 684 °C, respectively. The soot oxidation performances of the fiber web types were

significantly greater than those of the LSCF bulk types (Fig. 5a and Table 1). In comparison, the T_{ig} values of LSCF6428-web, LSCF7328-

web and LSCF8228-web were determined to be 397, 403 and 413 °C, respectively. According to the enlarged DTA graphs (Fig. 5a, inset), two maximum points of lower ($T_{\max,L}$) and higher ($T_{\max,H}$) temperature were observed at the $T_{\max,L}$ values of 490, 494 and 505 °C and the $T_{\max,H}$ values of 585, 590 and 597 °C for LSCF6428-web, LSCF7328-web and LSCF8228-web, respectively. This result implies that the lower maximum temperature ($T_{\max,L}$) was related to the catalytic reaction by the contact effect between the soot on the catalyst surface, whereas the higher maximum temperature ($T_{\max,H}$) was associated with the oxidation of the loose-contacted soot particles that were situated in the interspaces within the web structure, as confirmed above. In addition, the T_f values for LSCF6428-web, LSCF7328-web and LSCF8228-web were 647, 650 and 655 °C, respectively. As a result, the higher catalytic activity of the LSCF web type is most likely due to the expanded contact area and the interior space with 3D structure, where soot particles are effectively captured.

As the Sr doping at the A site was increased, lower T_{\max} temperatures were found, which indicates a higher catalytic activity with greater Sr incorporation into the perovskite lattice. This trend is presumably because the oxygen vacancy increased with the increase of Sr doping [44–46]. Thus, this unique web structure may promote soot oxidation, and the schematics account for the correlation with the surface SEM images (Fig. 5c). In contrast, under the TC mode, although the T_{\max} values of the bulk types slightly decreased by approximately 10.3 °C on average, overall, similar performances were recorded, and only one of the T_{\max} peaks was observed for both the bulk and web types (see Supplementary Fig. S10), which is presumably because of exceeding the compact contact of the catalyst and soot [52].

To investigate the reactivity of oxygen species in the perovskite oxides, we carried out the temperature programmed reduction (TPR) of H_2 for LSCF6428-web and LSCF6428-bulk catalysts. H_2 consumption proceeded in the temperature range of 150–900 °C for both catalysts with several peaks (Fig. S11). The H_2 consumption for LSCF6428-web was higher than that for the LSCF6428-bulk at low temperature (250–500 °C) which is associated with the removal of nonstoichiometric surplus oxygen accommodated within the lattice [53]. This finding implies that the reactivity of the lattice oxygen species of the LSCF catalysts was improved by changing their morphologies. However, the changes in the reactivity of oxygen did not contribute to the soot oxidation performance because the temperatures for soot oxidation were almost comparable for the LSCF6428-web and LSCF6428-bulk catalysts under the TC mode (Fig. S10).

Fig. 6 shows the temperature programmed oxidation (TPO) profiles for CB combustion over LSCF6428-web and LSCF6428-bulk in the temperature range of 100–700 °C under dry and humid ($[H_2O] = 3\%$) conditions. In all cases, CO_2 was observed and no other C-containing products were detected. For LSCF6428-bulk, the CO_2 formation started at around 400 °C and the maximum temperatures for CO_2 emission under humid (3% H_2O) and dry conditions (0% H_2O) were observed at approximately 690 and 700 °C (Fig. 6a). On the other hand, those of LSCF6428-web were measured to be 640 and 680 °C, respectively (see Fig. 6b). Thus, the maximum temperatures for CB combustion were lower for LSCF6428-web than those for LSCF6428-bulk, confirming that morphological change from powder to web facilitated the CB combustion under both humid and dry conditions. The TPO profiles also revealed that the addition of water vapor to the reaction gases lowered the temperatures for soot oxidation, which is probably due to the elimination of adsorbed hydrogen by oxygen species and the increase in contact area caused by gasification of carbon with water [54]. It is worth to note that the crystalline structure of LSCF6428-web did not change after the TPO experiment (see Supplementary Fig. S12), indicating that the catalyst exhibited high thermal stability.

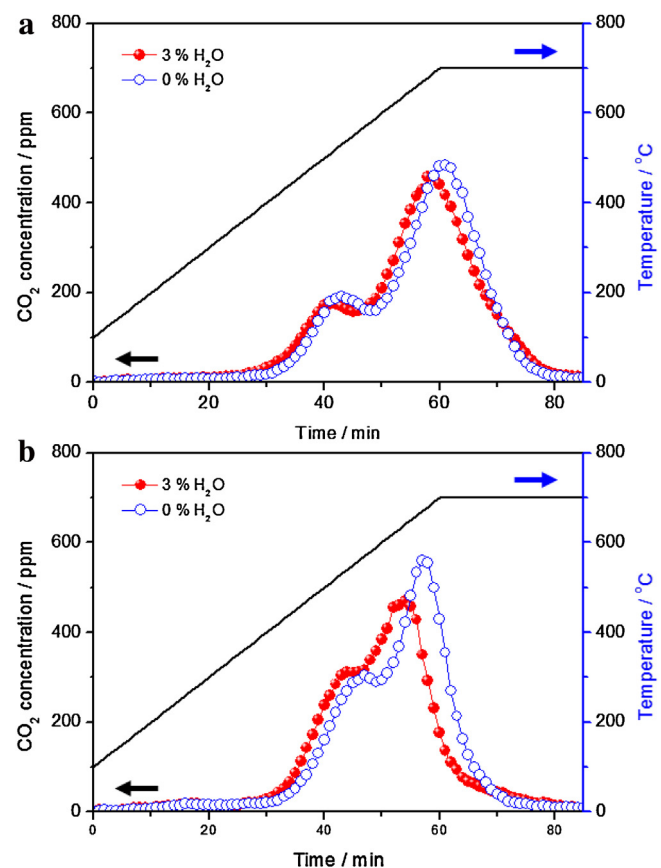


Fig. 6. TPO profiles of soot and catalyst mixture (loose contact). (a) LSCF6428-bulk (b) LSCF6428-web. Feeding condition: 6% O_2 , 3% H_2O or 0% H_2O ; gas flow: 100 $mL\ min^{-1}$; heating rate: 10 $^{\circ}C\ min^{-1}$.

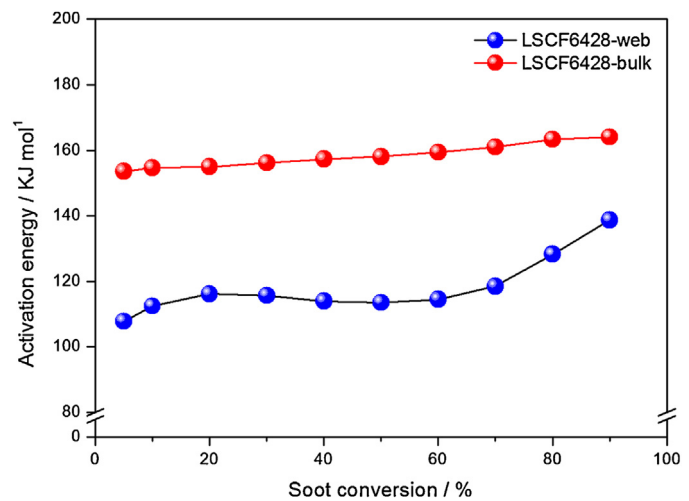


Fig. 7. Activation energies of LSCF6428-web and LSCF6428-bulk.

The activation energy (ΔE) of catalytic activity is useful to study the process and mechanism of catalytic reactions. Accordingly, we evaluated the activation energy of LSCF6428-web and LSCF6428-bulk by using Ozawa plots from the TGA curves (Supplementary Fig. S13). The activation energies of LSCF6428-bulk were calculated to be from 153.5 to 164.0 kJ mol⁻¹, whereas those of LSCF6428-web were measured to range from 107.8 to 138.7 kJ mol⁻¹ under the LC mode (Fig. 7). The activation energy of LSCF6428-web was found to be lower than that of LSCF6428-bulk, thus indicating higher catalytic activity for LSCF6428-web than LSCF6428-bulk. Furthermore,

the activation energy of LSCF6428-bulk exhibited a modest increase in the range of 5–90%, whereas that of the LSCF6428-web exhibited a relatively rapid rise from 60%. By comparing the soot oxidation (Fig. 5), the two measured maximum peaks of LSCF6428-web in the TG and DTA curves imply that the lower peak ($T_{\max,L}$) is attributable to the oxidation of soot particles that are adjacent to the surface. In contrast, the higher peak ($T_{\max,H}$) is attributable to the reaction of contactless soot from the surface of the catalyst, which is presumably due to the 3D web structure.

We have reported that in the catalytic soot oxidation over K-containing perovskite oxide series, $\text{La}_{1-x}\text{K}_x\text{MnO}_3$, catalyst surface area and surface concentration of active species were the important factors controlling the catalytic performance [55]. The results described above gave us the evidence that the morphological structures of perovskite oxides also affect the catalytic soot oxidation performance: the soot combustion with fiber-web catalyst proceeded at lower temperature than that with powder catalyst, which reflected the ratio of catalytic soot oxidation process to non-catalytic oxidation process. Since the soot oxidation mainly takes place at the triple phase boundary (TPB) of a solid reactant (soot), a catalyst and a gaseous reactant (O_2), the contact points or conditions between soot particle and active sites (TPB) are considerably important for soot oxidation (solid-solid reaction) [56]. Therefore, the web type catalyst is effective for soot oxidation because the increased contact points can accelerate catalytic soot oxidation processes.

4. Conclusions

In summary, $\text{La}_{1-x}\text{Sr}_x\text{Co}_{0.2}\text{Fe}_{0.8}\text{O}_{3-\delta}$ perovskite oxide fibrous webs were prepared by an electrospinning method and used for catalytic soot oxidation. The synthesized $\text{La}_{1-x}\text{Sr}_x\text{Co}_{0.2}\text{Fe}_{0.8}\text{O}_{3-\delta}$ perovskite oxide fibrous webs have a 3D structure that consists of large pores (approximately 1–90 μm macro-pores) compared with the $\text{La}_{1-x}\text{Sr}_x\text{Co}_{0.2}\text{Fe}_{0.8}\text{O}_{3-\delta}$ perovskite bulk types. From the results of the morphology and 3D analysis, the improved catalytic performance could be attributed to the considerable increase in the number of contact points between the reactant (soot) and the surface of the catalyst, resulting from the 3D large-pore structure, which can hold the soot particles. This unique feature provides higher soot combustion activity with a much lower activation energy. The contact area is an important factor for catalytic soot oxidation because the increased contact area is able to increase the catalytic activity. Our results suggested that the perovskite oxides with fiber web structures are promising as the soot oxidation catalysts.

Acknowledgements

This article is dedicated to the memory of the late Professor Y. Teraoka, who passed away unexpectedly on July 2, 2014. We would like to express our sincere respect and gratitude to his exceptional contributions towards the study of catalysis and perovskites. Industrial Technology Innovation Program funded by the Ministry Of Trade, Industry and Energy (MOTIE), Republic of Korea (grant number 10052076).

Appendix A. Supplementary data

Supplementary data associated with this article can be found, in the online version, at <http://dx.doi.org/10.1016/j.apcatb.2016.03.001>.

References

- [1] D.W. Dockery, Ann. Epidemiol. 19 (2009) 257.
- [2] K. Vaaraslahti, A. Virtanen, J. Ristimäki, J. Keskinen, Environ. Sci. Technol. 38 (2004) 4884.
- [3] E. Obeid, L. Lizarraga, M.N. Tsampas, A. Cordier, A. Boréave, M.C. Steil, G. Blanchard, K. Pajot, P. Vernoux, J. Catal. 309 (2014) 87.
- [4] B.A.A.L. van Setten, M. Makkee, J.A. Moulijn, Catal. Rev. 43 (2001) 489.
- [5] Z. Liu, A.N. Shah, Y. Ge, Y. Ding, J. Tan, L. Jiang, L. Yu, W. Zhao, C. Wang, T. Zeng, J. Environ. Sci. 23 (2011) 798.
- [6] K. Krishna, A. Bueno-López, M. Makkee, J.A. Moulijn, Appl. Catal. B: Environ. 75 (2007) 189.
- [7] I. Atribak, A. Bueno-López, A. García-García, J. Catal. 259 (2008) 123.
- [8] J. Liu, Z. Zhao, J. Lan, C. Xu, A. Duan, G. Jiang, X. Wang, H. He, J. Phys. Chem. C 113 (2009) 17114.
- [9] M.V. Twigg, Appl. Catal. B: Environ. 70 (2007) 2.
- [10] B. Białobok, J. Trawczyński, T. Rzadki, W. Miśta, M. Zawadzki, Catal. Today 119 (2007) 278.
- [11] D. Fino, E. Cauda, D. Mescia, N. Russo, G. Saracco, V. Specchia, Catal. Today 119 (2007) 257.
- [12] L. Castoldi, R. Matarrese, L. Lietti, P. Forzatti, Appl. Catal. B: Environ. 90 (2009) 278.
- [13] W.F. Shangguan, Y. Teraoka, S. Kagawa, Appl. Catal. B: Environ. 12 (1997) 237.
- [14] L. Xue, C. Zhang, H. He, Y. Teraoka, Appl. Catal. B: Environ. 75 (2007) 167.
- [15] Y. Teraoka, K. Nakano, W. Shangguan, S. Kagawa, Catal. Today 27 (1996) 107.
- [16] H. Shimokawa, H. Kusaba, H. Einaga, Y. Teraoka, Catal. Today 139 (2008) 8.
- [17] Z. Li, M. Meng, Y. Zha, F. Dai, T. Hu, Y. Xie, J. Zhang, Appl. Catal. B: Environ. 121–122 (2012) 65.
- [18] M.A. Peña, J.L.G. Fierro, Chem. Rev. 101 (2001) 1981.
- [19] L. Sui, L. Yu, Y. Zhang, Energy Fuels 20 (2006) 1392.
- [20] Y. Teraoka, K. Kanada, S. Kagawa, Appl. Catal. B: Environ. 34 (2001) 73.
- [21] F.E. López-Suárez, a. Bueno-López, M.J. Illán-Gómez, B. Ura, J. Trawczynski, Top. Catal. 52 (2009) 2097.
- [22] N. Yamazoe, Y. Teraoka, Catal. Today 8 (1990) 175.
- [23] Y. Teraoka, H.-M. Zhang, S. Furukawa, N. Yamazoe, Chem. Lett. 14 (1985) 1743.
- [24] Y. Teraoka, H.-M. Zhang, N. Yamazoe, Chem. Lett. 14 (1985) 1367.
- [25] Y. Teraoka, T. Nobunaga, N. Yamazoe, Chem. Lett. 17 (1988) 503.
- [26] Y. Teraoka, H.M. Zhang, K. Okamoto, N. Yamazoe, Mater. Res. Bull. 23 (1988) 51.
- [27] Z. Zhong, K. Chen, Y. Ji, Q. Yan, App. Catal. A: Gen. 156 (1997) 29.
- [28] T. Screen, Platin. Met. Rev. 51 (2007) 87.
- [29] B.R. Stanmore, J.F. Brilhac, P. Gilot, Carbon N.Y. 39 (2001) 2247.
- [30] K. Villani, C.E.A. Kirschhock, D. Liang, G. Van Tendeloo, J.A. Martens, Angew. Chemie Int. Ed. 45 (2006) 3106.
- [31] G. Zhang, Z. Zhao, J. Liu, G. Jiang, A. Duan, J. Zheng, S. Chen, R. Zhou, Chem. Commun. 46 (2010) 457.
- [32] Y. Wei, J. Liu, Z. Zhao, Y. Chen, C. Xu, A. Duan, G. Jiang, H. He, Angew. Chem. Int. Ed. 50 (2011) 2326.
- [33] Y. Wei, J. Liu, Z. Zhao, A. Duan, G. Jiang, C. Xu, J. Gao, H. He, X. Wang, Energy Environ. Sci. 4 (2011) 2959.
- [34] E. Aneggi, D. Wiater, C. de Leitenburg, J. Llorca, A. Trovarelli, ACS Catal. 4 (2014) 172.
- [35] P. Miceli, S. Bensaid, N. Russo, D. Fino, Nanoscale Res. Lett. 9 (2014) 1.
- [36] C. Lee, J.-I. Park, Y.-G. Shul, H. Einaga, Y. Teraoka, Appl. Catal. B: Environ. 174–175 (2015) 185.
- [37] C. Gong, C. Song, Y. Pei, G. Lv, G. Fan, Ind. Eng. Chem. Res. 47 (2008) 4374.
- [38] Y. Dai, W. Liu, E. Formo, Y. Sun, Y. Xia, Polym. Adv. Technol. 22 (2011) 326.
- [39] T. Ozawa, J. Therm. Anal. 2 (1970) 301.
- [40] T. Ozawa, Bull. Chem. Soc. Jpn. 38 (1965) 1881.
- [41] D. Waller, J.A. Lane, J.A. Kilner, B.C.H. Steele, Mater. Lett. 27 (1996) 225.
- [42] M. Machkova, N. Brashkova, P. Ivanov, J.B. Carda, V. Kozhukharov, Appl. Surf. Sci. 119 (1997) 127.
- [43] J.N. Kuhn, U.S. Ozkan, J. Catal. 253 (2008) 200.
- [44] H. Ullmann, N. Trofimko, F. Tietz, D. Stöver, A. Ahmad-Khanlou, Solid State Ionics 138 (2000) 79.
- [45] J. Mizusaki, I. Yasuda, J. Shimoyama, S. Yamauchi, K. Fueki, J. Electrochem. Soc. 140 (1993) 467.
- [46] J.A. Kilner, R.A. De Souza, I.C. Fullarton, Solid State Ionics 86–88 (1996) 703.
- [47] N.A. Seaton, Chem. Eng. Sci. 46 (1991) 1895.
- [48] J.P.A. Neef, M. Makkee, J.A. Moulijn, Appl. Catal. B: Environ. 8 (1996) 57.
- [49] Z. Zhao, A. Obuchi, J. Uchisawa, A. Ogata, S. Kushiyama, Chem. Lett. 27 (1998) 367.
- [50] H. Wang, Z. Zhao, C. Xu, J. Liu, Catal. Lett. 102 (2005) 251.
- [51] P. Gilbert, J. Theor. Biol. 36 (1972) 105.
- [52] H. Shimokawa, Y. Kurihara, H. Kusaba, H. Einaga, Y. Teraoka, Catal. Today 185 (2012) 99.
- [53] S. Ponce, M.A. Peña, J.L.G. Fierro, Appl. Catal. B: Environ. 24 (2000) 193.
- [54] A.F. Ahlström, C.U. Odenbrand, Carbon 27 (1989) 475.
- [55] H. Shimokawa, H. Kusaba, H. Einaga, Y. Teraoka, Bull. Chem. Soc. Jpn. 88 (2015) 1486.
- [56] J.V. Craenenbroeck, D. Andreeva, T. Tabakova, K.V. Werde, J. Mullens, F. Verpoort, J. Catal. 209 (2002) 515.